Simon Desrochers
Dassault Systèmes Inc.,
393 Saint-Jacques Street,
Montreal, QC, H2Y 1N9, Canada
e-mail: simon.desrochers@3ds.com

Damiano Pasini
Mem. ASME
Department of Mechanical Engineering,
McGill University,
3480 University Street,
Montreal, QC, H3A 2A7, Canada
e-mail: damiano.pasini@mcgill.ca

Jorge Angeles
ASME Fellow
Department of Mechanical Engineering,
McGill University,
817 Sherbrooke Street West,
Montreal, QC, H3A 2K6, Canada
e-mail: angeles@cim.mcgill.ca

Optimum Design of a Compliant Uniaxial Accelerometer

This work focuses on the multi-objective optimization of a compliant-mechanism accelerometer. The design objective is to maximize the sensitivity of the accelerometer in its sensing direction, while minimizing its sensitivity in all other directions. In addition, this work proposes a novel compliant hinge intended to reduce the stress concentration in compliant mechanisms. The paper starts with a brief description of the new compliant hinge, the Lamé-shaped hinge, followed by the formulation of the aposteriori multi-objective optimization of the compliant accelerometer. By using the normalized constrained method, an even distribution of the Pareto frontier is found. The paper also provides several optimum solutions on a Pareto plot, as well as the CAD model of the selected solution. [DOI: 10.1115/1.4001002]

1 Introduction

Accelerometers are inertial sensors, which provide an output proportional to acceleration. These sensors can be extensively applied in industries. In addition to the technical test measurement and modal analysis, accelerometers are now commonly used in many fields such as the automotive industry, aero- and astronautical industries, military industry, robotic systems, medical instruments, video cameras, free-space pointers, and so on [1]. For example, accelerometers are used in automobile crash tests or guidance systems. Guidance systems made of accelerometers are called inertial navigation system (INS).

The vast majority of accelerometers function on the principle of the mass-spring system. The mass, which is referred to as the proof-mass or seismic mass, is elastically suspended on the accelerometer frame. The elastic suspension is realized by means of flexible beams or compliant hinges. Regarding uniaxial accelerometers, the resulting compliant mechanism is designed to allow the proof-mass to translate exclusively along one direction. This is referred to as the sensitive direction. Figure 1 represents the mass-spring system of a uniaxial accelerometer whose sensitive direction is that of the x-axis. The resulting proof-mass displacement yields a signal that is linearly related to the acceleration component in the sensitive direction. It is common practice to refer to the sensitive direction as the *sensitive axis*.

The bias errors of inertial measurements come from the off-axis sensitivity of the mechanism [2]. From a mechanical viewpoint, off-axis sensitivity corresponds to the parasitic motion emerging when the accelerometer is subjected to angular acceleration, or when acceleration is not parallel to the sensitive axis. Therefore, in order to reduce the bias errors, the off-axis stiffness of the proof-mass suspension must be increased. The frequency range of accelerometers is quite broad, extending from a few Hertz to several kiloHertz. The high-frequency response is limited by the resonance of the seismic mass of the accelerometer mass-spring system. Resonance produces a high peak in response to the natural frequency λ_n, which is usually somewhere near 1000 Hz for low-frequency accelerometers (Fig. 2). Accelerometers are ordinarily usable up to about 1/3 of their natural frequency [2]. Data above this frequency will be affected by the resonant response, but may be used if the effect is factored in properly. Since the usable frequency of low-frequency accelerometers ranges from 0 Hz to 600 Hz, the natural frequency should not exceed 1800 Hz.

Low-frequency accelerometers often have the advantage of being highly sensitive [3,4]. Their mechanical structure is fragile and displays high off-axis sensitivity. Consequently, commonly used low frequency accelerometers have a limited range of acceleration, and an off-axis sensitivity of approximately 5%. To override the low off-axis stiffness of serial architectures, researchers have developed parallel architectures offering superior properties compared to a simple cantilever beam.

In this paper, we build on the compliant realization of the simplicial uniaxial accelerometer (SUA) proposed by Cardou et al. [5]. According to Lobontiu [6], a compliant mechanism is "a mechanism that is composed of at least one flexible component that is sensibly deformable compared to other rigid links." Therefore, compliant mechanisms generate work by using the deflection of their flexible components instead of using conventional joints. From a fabrication perspective, compliant mechanisms can be classified into two categories. The first category, micromachined mechanisms, is limited to planar mechanisms due to the unidirectional nature of the etching process used in micromachining [2]. The second category comprises the compliant realization of millimeter-scale three-dimensional mechanisms.

We can cite two main advantages of a compliant realization for the design of accelerometers. First, there is a reduction in cost as a result of element reduction. Second, compliant accelerometers provide upgraded performance, due to reduced wear, maintenance, and weight [7]. However, compliant mechanisms have four main drawbacks that can affect the performance of the mechanism, some appearing also in accelerometers at large, as follows: limited sensitivity, off-axis sensitivity, axis drift, and stress concentration [8]. The output of the accelerometer is a signal proportional to the relative displacement of the proof-mass with respect to the object on which the accelerometer is mounted. Therefore, the sensitivity of the accelerometer is limited by the joint stiffness, as the joint restrains the proof-mass displacement when subjected to an acceleration parallel to the sensitive axis. On the other hand, the off-axis sensitivity resulting from the parasitic off-axis bending of the compliant joint should be minimized if the accelerometer is to be insensitive to parasitic off-axis acceleration. The axis drift is gov-

Contributed by the Mechanisms and Robotics Committee of ASME for publication in the JOURNAL OF MECHANICAL DESIGN. Manuscript received January 24, 2009; final manuscript received December 19, 2009; published online April 22, 2010. Assoc. Editor: Mary Frecker.

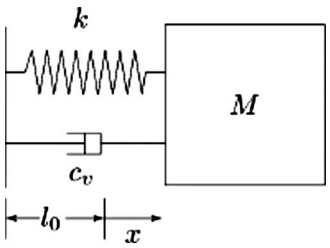

Fig. 1 Mass-spring system of an accelerometer

erned by the motion precision of the proof-mass. In a device subject to axis drift, the proof-mass may undesirably move out of its axis of motion. Finally, stress concentration affects the life and range of motion of the device.

The range of motion can be measured by the "mechanical advantage," which is dimensionless and defined as [6,9]

$$m.a. = \frac{|u_{\text{out}}|}{|u_{\text{in}}|} \tag{1}$$

where u_{in} and u_{out} are the input and output displacements. Since the readout of the accelerometer is a relative displacement, we adapted the foregoing concept to our needs, and produced the *mechanical sensitivity* of a compliant accelerometer, to be defined in Eq. (12).

Several optimization techniques are used in the design of compliant mechanisms. A popular strategy is topology optimization, which can find the distribution of a given amount of material that maximizes the stiffness of the structure [9–13]. In the compliant design, the technique was first used to generate the architecture of optimum planar mechanisms. The problem with the resulting mechanism, however, is that it does not consider the sensitivity to out-of-plane forces. Furthermore, this optimization technique cannot be used to find the optimum shape of a desired layout, since it generates its own layout.

The design technique introduced in this work does not generate optimum layouts, but optimizes the dimensions of a given layout. Thus, the designer is free to optimize any preselected three-dimensional compliant mechanism layout. Moreover, the technique minimizes the parasitic compliance in all off-axis directions. To do so, aposteriori multi-objective optimization is used to find the best trade-off between conflicting objective criteria of the compliant mechanism. Among the multi-objective optimization techniques, we have chosen the normalized normal constraint method (NNCM) to obtain an evenly distributed Pareto frontier [14].

Before applying multi-objective optimization to the uniaxial accelerometer, we start with a structural optimization of the compliant realization of the accelerometer. As stated in Refs. [8,15], one of the main drawbacks of a compliant hinge is the high stress concentration leading to low fatigue strength. The stress concentration depends on the stress distribution, which is controlled by the change in curvature of the beam. In this paper, we propose the Lamé curves to improve the curvature distribution of the original compliant hinge profile. The same method is then applied to an evolved realization of the uniaxial accelerometer proposed in Ref. [16].

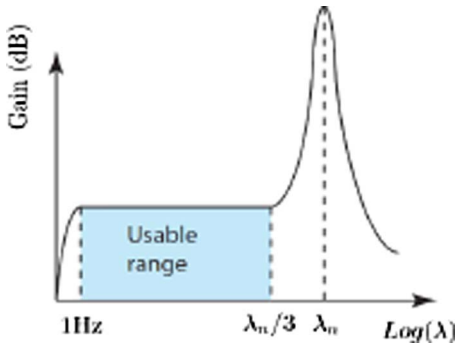

Fig. 2 Frequency response

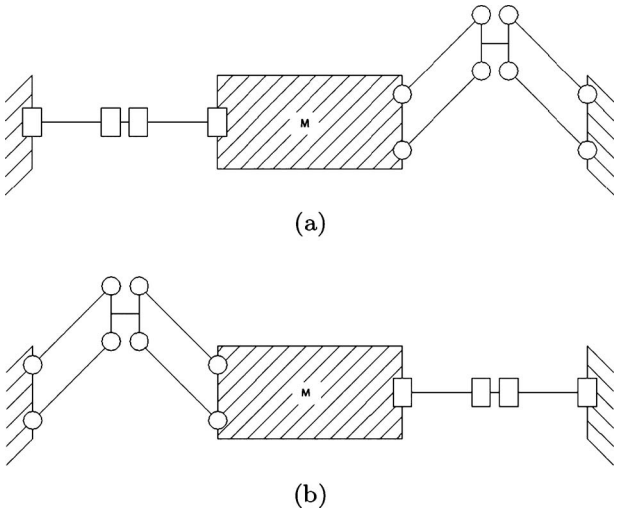

Fig. 3 The simplicial 2 IIII uniaxial accelerometer: (*a*) top view; (*b*) front view

2 Architecture of the Accelerometer

The simplicial architecture for a multi-axial accelerometer, as proposed in Ref. [16] refers to isotropic mechanism architectures proper of parallel-kinematics machines (PKMs), allowing the measurement of one, two, or three acceleration components. Here, Cardou and Angeles [16] characterized the architecture as simplicial since the proof-mass is suspended by $n+1$ legs, where n is the number of acceleration components measured by the accelerometer, with $n=1,2,3$. The set of $n+1$ legs form the vertices of a simplex[1] created by the leg attachment points of the n-dimensional accelerometer. The simplexes corresponding to one, two, and three dimensions are the line, the triangle, and the tetrahedron. If the triangle and the tetrahedron are equilateral, then the accelerometer is equally sensitive in all the sensitive directions, thereby making the accelerometer isotropic. Furthermore, the accelerometers always have one more leg than their dimension requires, thereby providing redundancy, which considerably adds robustness against measurement error.

The SUA at hand is intended to measure point-acceleration along one direction [16]. To constrain the mass to move along a single axis, we use a IIII-leg architecture, where a Π joint is a parallelogram linkage, as described in detail in Ref. [18], thereby obtaining a novel realization of the well-known Sarrus mechanism. A planar translation mechanism can be obtained by coupling two Π-joints together. The intersection of the two leg-planes forms the new one-dimensional motion line of the mechanism. Therefore, suspending the proof-mass to each leg on both vertices (Fig. 3) allows the one-dimensional motion of the proof-mass.

2.1 Compliant Realization of a Uniaxial Accelerometer. In this work, we propose a new compliant realization of a uniaxial accelerometer by replacing the articulated Π-joints of the SUA legs by compliant Π-joints. In a common compliant approximation of the Π-joint, two identical straight flexible beams cast at both ends lie parallel to each other to create a parallel-guiding

[1]In mathematical programming, a simplex is a polyhedron with the minimum number of vertices embedded in $\mathbb{R}^n$ [17].

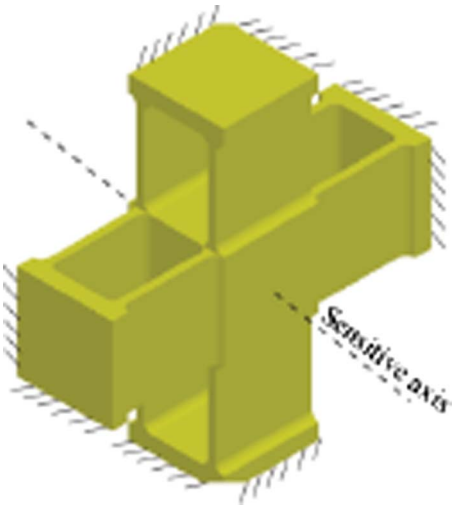

Fig. 4 Cross-configuration mechanism

mechanism, or parallelogram [19]. Indeed, the flexible mechanism has the shape of a parallelogram and allows only for translation in one direction. The new layout of the mechanism, as shown in Fig. 4, is not only a compact form of the uniaxial accelerometer, but also offers an excellent ratio of off-axis stiffness to sensitive-axis stiffness. Figure 5 illustrates the behavior of the new mechanism layout subjected to acceleration along the sensitive-axis direction. The mechanism works on the principle of large-displacement compliant joints developed by Moon et al. [8].

2.2 Material Selection. An important issue of compliant design is the material selection. Since accelerometers are designed to be high-precision instruments, we need to consider the predictability of the material properties. Metals are known to have predictable material properties, low susceptibility to creep, and predictable fatigue life. On the contrary, plastics and composites have a large variability in their mechanical properties, making them less predictable than metals. They are also sensitive to creep and stress relaxation, which could bring about problems in the presence of constant acceleration such as gravity. Therefore, titanium alloy was selected to build the accelerometer.

Not every fabrication process can produce titanium alloy structures. To cope with the issue of titanium manufacturing, the accelerometer will be built with the EOSINT M 270 machine tool for direct metal laser-sintering (DMLS). This machine can manufacture complex three-dimensional geometries in multiple types of metal, such as stainless steel, tool steel, or for the case of the accelerometers, TiAl6V4, a titanium alloy. The machine also has an excellent detail resolution of $\epsilon=100$ μm, with ϵ being the focus diameter of the laser. The precision of the DMLS machine allows the fabrication of a compact monolithic titanium accelerometer.

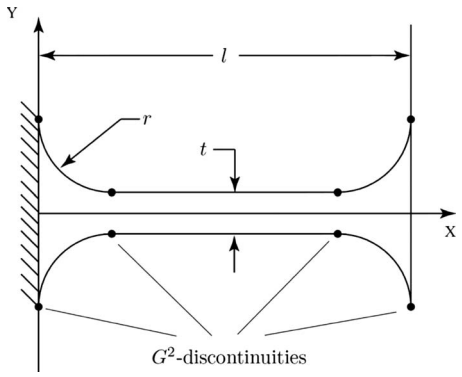

Fig. 6 Corner-filleted hinge

2.3 Lamé-Shaped Hinges. Straight flexible beams used for compliant mechanisms are integrated within a monolithic structure by adding a fillet at the interface between the beam and the rigid link. Thus, the resulting flexible beam is said to be a corner-filleted hinge. However, the circular profile of the fillets, which is the most common shape found in the literature [20,21], is not optimal with respect to the stress concentration because circular fillets give rise to G^2-discontinuities, i.e. discontinuities in the curvature of a geometric curve. It is known that curvature discontinuities in the structure profile generate stress concentrations [22–24]. The stress concentration resulting from the discontinuities of the corner-filleted hinge profile depicted in Fig. 6 can accelerate fatigue failure and reduce the life of the compliant mechanism [25]. What is proposed in this work is to optimize the fillet profile of the flexible beam by designing its shape with Lamé curves. By controlling the curvature of the fillet, the von Mises stress distribution becomes more even [26].

De Bona and Munteanu [15] proposed an optimum compliant hinge using a cubic-spline curve to find the best profile, which will maximize the flexibility of a compliant revolute joint. In this paper, we choose Lamé curves as opposed to other families of curves, e.g. splines, because of their simplicity.

2.3.1 Lamé Curves. Lamé curves are η-order curves defined by the equation

$$\left(\frac{x}{a}\right)^{\eta}+\left(\frac{y}{b}\right)^{\eta}=1 \tag{2}$$

where η can be any rational number. There are nine different types of Lamé curves based on the form of the exponent η [27]. For our study, we resort to $\eta>2$. From Eq. (2), it is apparent that Lamé curves are analytic everywhere; even-integer-powered curves are closed and doubly symmetric. For $\eta=2$, the curve results in a circle and, as η tends to infinity, the curve approaches a square. In the case of odd-integer-powered, as depicted in Fig. 7, the Lamé curves are open and extend infinitely toward an asymptote, crossing the second and fourth quadrants and passing through

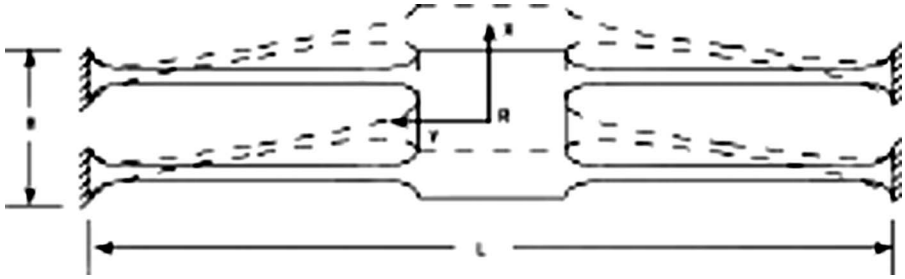

Fig. 5 Deformation along the sensitive axis

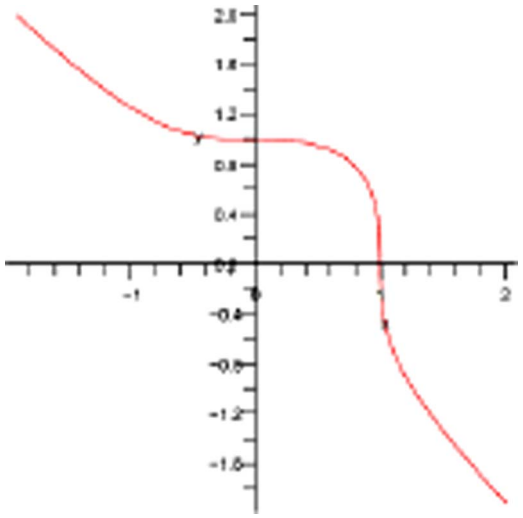

Fig. 7 Lamé curves for η=3

the origin. Fractional-powered Lamé curves are also open and analytic in the first quadrant, but in the other quadrants, Eq. (2) leads to complex coordinates.

In order to obtain a closed curve for any rational power η, Eq. (2) is modified to read

$$\left|\frac{x}{a}\right|^{\eta} + \left|\frac{y}{b}\right|^{\eta} = 1 \tag{3}$$

Figure 8 shows the curves obtained using Eq. (3) for η=2, 3.5, 5, 8, and 30. Absolute-value bars are essential for all the rational-powered curves, but can be deleted for their even-integer-powered counterparts. Absolute values, however, introduce discontinuities in the curvature because the absolute-value function is not differentiable at the origin.

As the curves shown in Fig. 8 have double symmetry, it is sufficient to study only the first quadrant of the curves for the generation of the fillets. Therefore, the curves that generate the fillets take the form

$$f(x,y) = \left(\frac{x}{b_x}\right)^{\eta} + \left(\frac{y}{b_y}\right)^{\eta} - 1 = 0 \tag{4}$$

for $2 < \eta \in \mathbb{Q}, x, y \in \mathbb{R}^+$, where $\mathbb{Q}$ is the set of rational numbers,

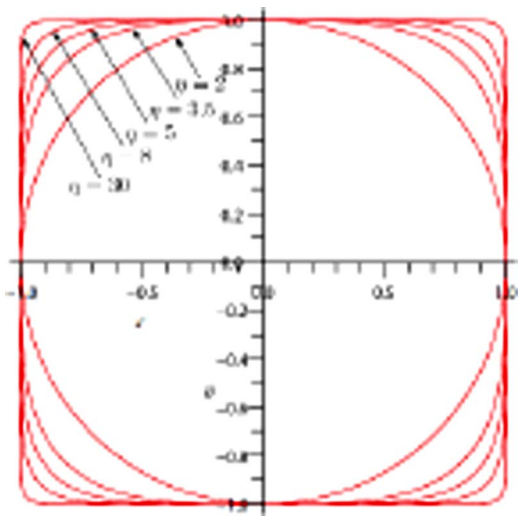

Fig. 8 Lamé curves of Eq. (3)

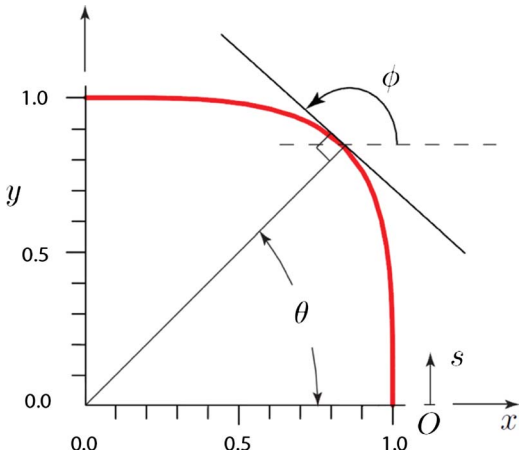

Fig. 9 Lamé curves polar coordinate for η=4

and b_x and b_y being the scaling parameters.

With regard to Eq. (4), the curve can be defined in terms of a parameter θ as

$$x(\theta) = \frac{1}{(1+\tan\theta^{\eta})^{1/\eta}}, \quad y(\theta) = \frac{\tan\theta}{(1+\tan\theta^{\eta})^{1/\eta}} \tag{5}$$

where the angle $\theta \in [0, \pi/2]$ is the polar coordinate of one point of the curve, measured with respect to the x-coordinate axis, and is defined positive counterclockwise. To generate the shape of the fillets, affine transformations are used to scale the coordinates x_1 and y_1 by means of parameters b_x and b_y, namely

$$x_1(\theta) = \frac{b_x}{(1+\tan\theta^{\eta})^{1/\eta}}, \quad y_1(\theta) = \frac{b_y \tan\theta}{(1+\tan\theta^{\eta})^{1/\eta}} \tag{6}$$

By using the new fillet to merge the flexible beams to the rigid links, a new type of compliant joint is created, which we call the Lamé-shaped hinge.

2.3.2 Curvature of the Lamé Curves. The advantage of this family of curves is that, for $\eta > 2$, their curvature vanishes at the intersections with the coordinate axes. The curvature $\kappa(s)$ is defined as

$$\kappa(s) \equiv \frac{d\phi}{ds} \tag{7}$$

where ϕ is the angle made by the tangent with a fixed line and s is the curve length, as shown in Fig. 9. From its definition, curvature has units of inverse length. If the Lamé curve is given by the parametric form of Eq. (5), then the curvature $\kappa(\theta)$ takes the form

$$\kappa(\theta) = \frac{x'(\theta)y''(\theta) - y'(\theta)x''(\theta)}{(x'(\theta)^2 + y'(\theta)^2)^{3/2}} \tag{8}$$

Notice that for $\eta > 2$, $\kappa(\theta)$ becomes undefined at θ=0 and $\pi/2$, but the continuity of the curvature at points (1,0) and (0,1) can be shown to be preserved by computing the limit of $\kappa(\theta)$ as θ approaches 0 or $\pi/2$, i.e.

$$\lim_{\substack{\theta\to 0 \\ \eta>2}} \kappa(\theta) = \lim_{\substack{\theta\to \pi/2 \\ \eta>2}} \kappa(\theta) = 0 \tag{9}$$

The curvature can be expressed in a more robust form, namely, implicit [28], as appearing in Eq. (4); whence

$$\kappa(x,y) = \frac{2f_{xy}f_xf_y - f_{xx}f_y^2 - f_{yy}f_x^2}{(f_x^2 + f_y^2)^{3/2}} \tag{10}$$

where standard notation for partial derivatives has been used. For the curve $f(x,y)$ of Eq. (4) the curvature takes the form [29]

$$\kappa(x,y) = \frac{(\eta-1)(xy)^{\eta-2}(x^{\eta}+y^{\eta})}{(x^{2\eta-2}+y^{2\eta-2})^{3/2}} \tag{11}$$

whence, apparently, the curvature of the rational-powered Lamé curves vanishes at the intersections with the coordinate axes. Thus, Lamé-shaped fillets as alternatives to the original circular fillets might be worthwhile because the new design improves the stress distribution around the fillets by providing G^2-continuity along the hinge profile.

3 Optimum Design

Once the layouts of the accelerometer and the compliant joint profile has been defined, we need to find the architecture that optimizes the accelerometer behavior.

3.1 The Optimization Methodology. This section describes the method used to find an optimum accelerometer architecture that minimizes the error of the measured acceleration. This error can be minimized by optimizing the sensitivity and natural frequencies of the compliant mechanism. The mechanical sensitivity evaluates the input-to-output amplification. In the field of compliant mechanisms, the input-to-output amplification ratio is called the "mechanical advantage," as recalled in Eq. (1), where u_{in} and u_{out} are the input and output displacements. Regarding accelerometers, the output displacement is not generated by an input displacement but by an input acceleration (a_{in}). Hence, we define here the mechanical sensitivity of a compliant accelerometer as

$$\Upsilon(\mathbf{x}) = \frac{|u_{\text{out}}(\mathbf{x})|}{|a_{\text{in}}|} \tag{12}$$

On the other hand, a minimum parasitic compliance in the plane normal to the sensitive axis, which is inversely proportional to the second natural frequency λ_s, can be obtained by minimizing the ratio between the first and second natural frequencies. In other words, the ratio tells how rigid the structure is in the direction normal to the sensitive axis. Finally, the axis drift needs to be taken into account only when the stiffness of the plane orthogonal to the sensitive axis is not isotropic. In the case of anisotropic stiffness, the resulting inertia forces acting on the system will not be balanced and will make the proof-mass deflect outside its translation trajectory. Designers need to ensure elastic isotropy in the normal plane[2] by suitably specifying the layout of the accelerometer. Thus, the optimization problem can be described as

$$f(\mathbf{x}) \equiv \begin{bmatrix} 1/|\Upsilon(\mathbf{x})| \\ \lambda_l(\mathbf{x})/\lambda_s(\mathbf{x}) \end{bmatrix} \rightarrow \min_x \tag{13}$$

subject to boundary constraints

$$x_j^l \le x_j \le x_j^h \tag{14}$$

and the design constraints

$$g_1(\mathbf{x}) \le 0, \quad g_2(\mathbf{x}) \le 0 \tag{15}$$

where $g_1(\mathbf{x})$ and $g_2(\mathbf{x})$ need to be defined presently, and $\mathbf{x} \in \mathbb{R}^n$, where $\lambda_l(\mathbf{x})$ and $\lambda_s(\mathbf{x})$ are the first and second natural frequencies, respectively.

The boundary constraints (Eq. (14)) limit the geometric variables to acceptable values defined by the manufacturing process. On the other hand, the design constraints deal with the maximum design space and strength requirement of the mechanism. The first constraint of Eq. (15) is a limit to the volume L^2H defined by the length and width of the mechanism. The second constraint therein restricts the stress in the flexible element of the accelerometer to fall in a range of ± 1000 g of the measurable acceleration. Within this range, the mechanism strain is prevented from plastic deformation.

To compute for the objective functions (Eq. (13)) at every optimization iteration, a finite element solver was coupled with the optimization algorithm. To generate the finite element (FE) model at each iteration according to inputs of the multi-objective algorithm, a MATLAB procedure was implemented, using ANSYS as the simulation toolbox. This is feasible, since MATLAB can execute any program without interrupting its processing. Hence, ANSYS is integrated in the optimization loop.

3.2 Problem Formulation. To optimize the accelerometer architecture, seven parameters are introduced, which play the role of design variables, and arrayed in the design vector $\mathbf{x}$:

$$\mathbf{x} = \begin{bmatrix} w & e & t & l & b_x & b_y & \eta \end{bmatrix}^T \tag{16}$$

which represent the width and length of the proof-mass, the thickness and length of the compliant joint, and the height, length, and degree of the Lamé curve describing the fillet of the compliant hinges, respectively.

The symmetric configuration of the accelerometer rules out the axis drift of the compliant mechanism. Therefore, we have a bi-objective optimization, the objective functions being the sensitive- and off-axis stiffnesses. The optimization problem is defined as in Eq. (13), subject to the boundary constraints

$$0 \le x_1, \quad (4b_y + 2t) \le x_2 \tag{17a}$$

$$\epsilon \le x_3, \quad 0 \le x_4 \tag{17b}$$

$$0 \le x_5 \le l/2 \tag{17c}$$

$$2\epsilon \le x_6, \quad 2 < x_7 \tag{17d}$$

and the design constraints

$$g_1(\mathbf{x}) = \frac{(2l+w)^2 e}{L^2 H} - 1 \le 0 \tag{18a}$$

$$g_2(\mathbf{x}) = \max_{\nu}(\sigma_{vM}(\nu) - \sigma_{\text{adm}}) \le 0 \tag{18b}$$

where ν, σ_{vM} and σ_{adm} are, respectively, the node of the finite element model (FEM), the von Mises stress, and the admissible stress for the maximum acceleration of 1000 g.

The optimization problem is subjected to the boundary constraints imposed by the physical dimensions of the compliant mechanism, except for x_3 and x_6, which are limited by the DMLS machine tool resolution. Indeed, the joint thickness t cannot be smaller than the smallest focus diameter $\epsilon = 100$ μm. On the other hand, $g_1(\mathbf{x})$ describes the compactness, which is subject to an inequality constraint to limit the design space. This limit is identified by a box with a volume $L^2H = 10^3$ mm^3. Finally, to compute for the stress constraint $g_2(\mathbf{x})$ and the natural frequencies of the device, a MATLAB routine was implemented to call the FEA solver at each iteration. In the case of the stress constraint $g_2(\mathbf{x})$, we use a different mesh, which considers the symmetries of the accelerometer. Since the compliant joints are all equally loaded, we compute for the stress in only one hinge. The structural model can be simplified even more with a symmetric analysis of the compliant joint. Figure 10 shows the model used for the structural analysis and the plane subjected to an antisymmetry condition.[3] The displacements of the flexible beam left-end were set to zero, while, at the other end, the rotations and displacement in the neutral-axis direction were set to zero in order to respect the layout of the

[2]Elastic isotropy in a plane means that the stiffness matrix of the structure at hand has two identical eigenvalues, as this matrix is symmetric. This means, in turn, that any vector in the same plane is an eigenvector of the stiffness matrix of the structure in *all* directions of the plane.

[3]Recall that an antisymmetry condition applies when the geometry and load are symmetric and antisymmetric, respectively, with respect to an axis.

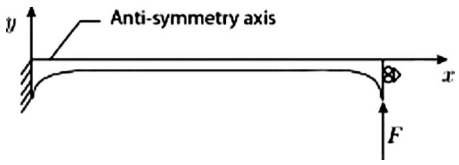

Fig. 10 Structural model

accelerometer. The load case is also depicted in Fig. 10, where the bending load is set to be

$$F = a_{\text{in}}\frac{m_p}{n} = \frac{1000gw^2e\rho}{8} \tag{19}$$

where a_{in}, m_p, n, g, and ρ are the maximum acceleration input, mass of the proof-mass, number of compliant links, gravity constant, and density of the titanium alloy, respectively.

To generate the FE model at each iteration according to inputs of the optimization algorithm, a MATLAB procedure was implemented, using ANSYS as the simulation toolbox. Hence, ANSYS can be completely implemented in the optimization loop. Furthermore, ANSYS automatically generates the mesh of the hinge at each iteration.

3.3 Multi-Objective Formulation. In general, the *i*th natural frequency of a structure is not an analytic function of the design parameters, which prevents us from using gradient-based methods of optimization. To overcome this issue, we use a direct method. In the field of optimization, the Nelder–Mead simplex algorithm [30] is a well-known effective method for direct-search optimization. The Nelder–Mead algorithm is modified and integrated in the intelligent moving object optimization algorithm (INTEMOB) [31] to handle nondifferentiable, discontinuous, and nonanalytic functions, as well as to deal with design constraints. For this reason, we used INTEMOB in this work.

Bearing in mind that the Nelder–Mead method is able to operate only on one objective function for minimization, we resort to multi-objective optimization, which is the process of simultaneously optimizing two or more conflicting objectives subject to the same constraints. As we have a bi-objective case, the feasible region of the design space is represented in a plot where the coordinate axes are the two objective functions, as depicted in Fig. 11. Multi-objective problems are known to have not one but many solutions, which form the Pareto optimal set or Pareto frontier. A Pareto solution is one where any improvement in one objective can only occur by worsening one or several objectives.

We selected the NNCM, as proposed by Messac et al. [14] because it generates a set of evenly spaced solutions on a normalized Pareto frontier. The method for the bi-objective case comprises seven steps, as follows:

Step 1: Anchor points. To normalize the two-dimensional Pareto frontier, we first need to find the two anchor points $\mu^{1\star}$ and $\mu^{2\star}$, which are the solutions minimizing both objectives independently. The line joining the two anchor points is called the Utopia line. The anchor points are obtained by solving problems PU1 and PU2 defined below, with the INTEMOB algorithm:

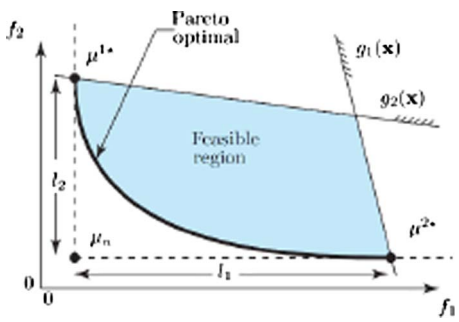

Fig. 11 Pareto frontier

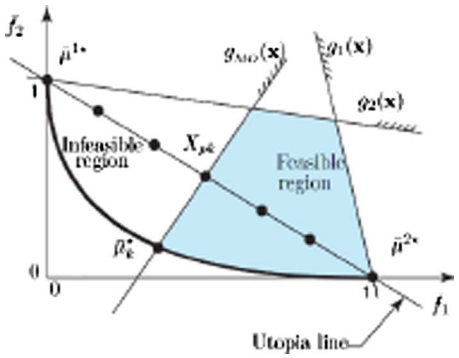

Fig. 12 Normalized Pareto frontier

Problem PUi $(i=1,2)$

$$f_i(\mathbf{x}) \to \min_{x} \tag{20}$$

subject to the boundary constraints

$$x_{lj} \le x_j \le x_{uj} \quad (j = 1,2,\ldots,N) \tag{21}$$

and the design constraints

$$g_1(\mathbf{x}) \le 0, \quad g_2(\mathbf{x}) \le 0 \tag{22}$$

with $f_1(\mathbf{x})$ and $f_2(\mathbf{x})$ defined as the first and second objective functions of Eq. (13), respectively.

Step 2: Objective mapping. To avoid scaling deficiencies, the optimization takes place in the normalized design objective space. The Utopia point μ_u in Fig. 11 is defined as

$$\mu_u = \{f_1(\mathbf{x}^{1\star}) \quad f_2(\mathbf{x}^{2\star})\} \tag{23}$$

and the distances l_1 and l_2 in Fig. 11 as

$$l_1 = f_1(\mathbf{x}^{2\star}) - f_1(\mathbf{x}^{1\star}) \quad l_2 = f_2(\mathbf{x}^{1\star}) - f_2(\mathbf{x}^{2\star}) \tag{24}$$

If $\bar{\mathbf{f}}$ is the normalized form of $\mathbf{f}$, the normalized design space displayed in Fig. 12 can be evaluated as

$$\bar{\mathbf{f}}(\mathbf{x}) = \left[\frac{f_1(\mathbf{x}) - f_1(\mathbf{x}^{1\star})}{l_1}, \quad \frac{f_2(\mathbf{x}) - f_2(\mathbf{x}^{2\star})}{l_2}\right]^T \tag{25}$$

Step 3: Utopia line vector. Define $\bar{\mathbf{n}}_u$ as the vector directed from $\bar{\mathbf{f}}(\mathbf{x}^{1\star})$ to $\bar{\mathbf{f}}(\mathbf{x}^{2\star})$, yielding

$$\bar{\mathbf{n}}_u = \bar{\mathbf{f}}(\mathbf{x}^{2\star}) - \bar{\mathbf{f}}(\mathbf{x}^{1\star}) \tag{26}$$

Step 4: Normalized increments. Compute for a normalized increment δ along the direction $\bar{\mathbf{n}}_u$ for a prescribed number of solutions m_1 as

$$\delta = \frac{1}{m_1 - 1} \tag{27}$$

Step 5: Generate Utopia line points. Evaluate a set of vectors $\bar{\mathbf{x}}_{pk}$, which define $\mathcal{X}_{pk}$ as the set of evenly distributed points on the Utopia line (Fig. 12), namely

$$\bar{\mathbf{x}}_{pk} = \iota_{1k}\bar{\mathbf{f}}(\mathbf{x}^{1\star}) + \iota_{2k}\bar{\mathbf{f}}(\mathbf{x}^{2\star}) \tag{28}$$

where

$$\iota_{1k} + \iota_{2k} = 1 \quad 0 \le \iota_{1k} \le 1 \tag{29}$$

Note that ι_{ik} is incremented by δ between 0 and 1 for $k \in \{1,2,\ldots,m_1\}$.

Step 6: Pareto point generation. Based on the new normalization we find the other m_1-2 Pareto solutions using the set of evenly distributed points on the Utopia line. For each point gen-

Table 1 Pareto solutions

k	Υ (nm/g)	$\frac{\lambda_l(x)}{\lambda_s(x)}$	w (mm)	e (mm)	t (mm)	l (mm)	b_x (mm)	b_y (mm)	η
1	40.12	0.1378	2.71	2.31	0.10	9.12	4.12	0.20	80/9
2	35.61	0.1056	4.57	2.62	0.10	7.45	3.37	0.20	7
3	27.92	0.0840	5.62	2.75	0.10	6.70	3.01	0.20	67/11
4	21.94	0.0713	5.51	3.21	0.10	6.01	2.71	0.20	23/4
5	16.72	0.0623	5.23	4.11	0.10	5.18	2.32	0.20	16/3
6	13.25	0.0540	4.91	4.92	0.10	4.82	2.19	0.20	5
7	10.97	0.0424	4.49	5.87	0.10	4.51	2.02	0.20	43/9

erated on the Utopia line, we solve for the following:

Problem Pk (for $k=2,3,4,\ldots,m_1-1$)

$$f_2(\mathbf{x}) \rightarrow \min_x \tag{30}$$

subject to the boundary constraints

$$x_{lj} \leq x_j \leq x_{uj} \quad j=1,2,\ldots,N \tag{31}$$

the design constraints

$$g_1(\mathbf{x}) \leq 0, \quad g_2(\mathbf{x}) \leq 0 \tag{32}$$

and the new multi-objective constraint

$$\bar{\mathbf{n}}_u^T(\bar{\mathbf{f}}(\mathbf{x}) - \bar{\mathbf{x}}_{pk}) \leq 0 \tag{33}$$

Step 7: Pareto design. Finally, the design solution that corresponds to each Pareto point can be evaluated in the design space by the relation

$$\mathbf{f}(\mathbf{x}_k) = [l_1\bar{f}_1(\mathbf{x}_k) + f_1(\mathbf{x}^{1\star}) \quad l_2\bar{f}_2(\mathbf{x}_k) + f_2(\mathbf{x}^{2\star})]^T \tag{34}$$

4 Results

To define the normalized Pareto optimal set, the two anchor points $\mu^{1\star}$ and $\mu^{2\star}$ were obtained by solving problems PU1 and PU2 described below, with the INTEMOB algorithm. At the optimum points $\mathbf{x}^{1\star}=[2.7\ 2.3\ 0.1\ 9.2\ 0.2\ 80/9]^T$ and $\mathbf{x}^{2\star}=[4.5\ 5.9\ 0.1\ 4.5\ 0.2\ 43/9]^T$, we found the two anchor points $\mu^{1\star}=(2.50\times10^7\ \ 0.1378)$ and $\mu^{2\star}=(9.17\times10^7\ \ 0.0452)$. Thus, the Utopia point results are $\mu_u=(2.50\times10^7\ \ 0.0452)$.

$$\text{Problem PU1:} \quad f_1(\mathbf{x}) \rightarrow \min_x \tag{35}$$

$$\text{Problem PU2:} \quad f_2(\mathbf{x}) \rightarrow \min_x \tag{36}$$

subject to Eqs. (17) and (18).

In addition to the anchor points, we need to find five additional solutions of the Pareto frontier to determine a total of seven points. Consequently, the interval distance on the Utopia line is equal to $\delta=0.1666$. The Pareto optimum solutions are listed in Table 1; Fig. 13 depicts the corresponding Pareto frontier.

The Pareto frontier gives us freedom to select a design architecture to meet specific conditions of the accelerometer. At one extreme, i.e., point 1, of the Pareto frontier, the fundamental frequency is the lowest and corresponds to the most sensitive accelerometer. At the other extreme, i.e., point 7, the frequency ratio $\lambda_l(\mathbf{x})/\lambda_s(\mathbf{x})$ is the minimum. The structural parameters that correspond to this point are the most appropriate for low parasitic-sensitivity accelerometers.

All the other points are intermediate optimum solutions. The seven Pareto solutions correspond to optimum accelerometers with different specifications. They are selected with respect to the weight factor related to the application of the accelerometer. As stated in Sec. 1, we aim at a general case where the accelerometer should have a natural frequency slightly higher than 1000 Hz and a ratio lower than 1/10. We select solution 4 in Fig. 13 as it is the first point that meets the two conditions. The fundamental frequency and the frequency ratio correspond to 1145 Hz and 0.0713, respectively. Figures 14 and 15 depict the stress distribution of solution 4 and the optimum accelerometer, respectively.

5 Discussion

The NNCM algorithm can generate a good approximation of the Pareto frontier with a small number of optimum solutions; this is a considerable advantage for mechanical systems with high computational complexity, such as those involving FEA calculations. In the problem at hand, only seven solutions were obtained to approximate well the Pareto frontier. The solutions are equally distributed along the Utopia line, as opposed to a priori multi-objective optimization methods, which need a larger number of points to represent the Pareto frontier.

The Pareto frontier helps the designer to select the best compromise among a set of optimum designs. In our case, we choose solution 4 as the resulting accelerometer meets the general characteristics of a low-frequency accelerometer with a usable frequency range that lies between 0 Hz and 600 Hz. Low-frequency accelerometers have the advantage of high sensitivity and good compactness; however, they have the disadvantages of very fragile mechanical structure and high off-axis sensitivity. Thus, com-

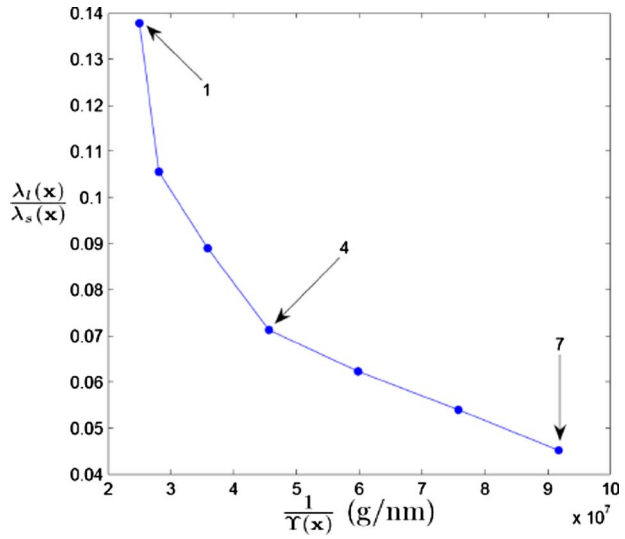

Fig. 13 Pareto frontier

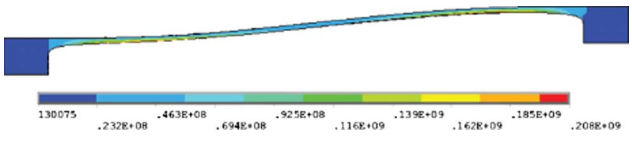

Fig. 14 von Mises stress distribution

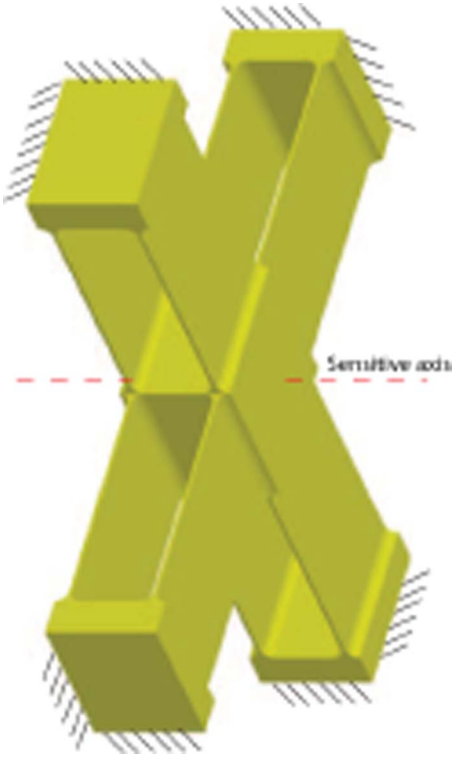

Fig. 15 Optimum accelerometer

monly used low-frequency accelerometers have a limited range of acceleration between 1 g and 50 g and high off-axis sensitivity of around 5%. To overcome these problems, the accelerometer architecture was optimized by considering these four characteristics. The first objective of the multi-objective optimization is to maximize the mechanical sensitivity (Y) of the accelerometer. However, by minimizing $1/Y$ and the frequency ratio λ_f/λ_s, the optimization also affects the accelerometer usable frequency range, which cannot exceed 1/3 of its fundamental frequency. Since the optimum accelerometer has a fundamental frequency of 1145 Hz, its usable frequency ranges from 0 Hz to 381 Hz. Moreover, the proposed compliant mechanism exhibits a low mechanical off-axis sensitivity through the minimization of the second objective. The resulting compliant mechanism is at least 1000 times more sensitive in its sensitive axis than in the other directions, which is a significant improvement. Finally, the optimization constraints allow the mechanism to fit in a box of $17.5 \times 17.5 \times 3.2$ mm^3, and prevent failure of the compliant mechanism under ± 1000 g.

6 Conclusions

The normalized normal constraint method was applied in the work reported here for the accelerometer design. Although only two objective functions were considered, the method can readily be extended to multiple objective functions. Since the objective functions are not analytic functions of the design parameters, the intelligent moving object algorithm, which is a direct optimization method, was integrated into the normalized normal constraint method. The method is intended to optimize a given layout, as opposed to topology optimization, which is used to generate the optimum layout. The method was applied to optimize the cross-configuration layout of a uniaxial accelerometer. However, the method can also be used to optimize triaxial accelerometers.

Acknowledgment

The support of Quebec's Fonds de recherche sur la nature et les technologies through Grant Nos. FQRNT PR-112531 and FQRNT PR-112531-Equip is highly acknowledged.

References

[1] MacDonald, G. A., 1990, "Review of Low Cost Accelerometers for Vehicle Dynamics," Sens. Actuators, A, **21**, pp. 303–307.
[2] Senturia, S., 2001, *Microsystem Design*, 3rd ed., Kluwer, Boston, MA.
[3] Yazdi, N., Najafi, K., and Salian, A. S., 2003, "A High-Sensitivity Silicon Accelerometer With a Folded-Electrode Structure," J. Microelectromech. Syst., **12**(4), pp. 479–486.
[4] Suna, C., Wang, C., and Fang, W., 2008, "On the Sensitivity Improvement of CMOS Capacitive Accelerometer," Sens. Actuators, A, **141**, pp. 347–352.
[5] Cardou, P., Pasini, D., and Angeles, J., 2008, "Lumped Elastodynamic Model for MEMS: Formulation and Validation," J. Microelectromech. Systems, **17**(4), pp. 948–961.
[6] Lobontiu, N., 2003, *Compliant Mechanisms: Design of Flexure Hinges*, CRC, Boca Raton, FL.
[7] Howell, L., 2001, *Compliant Mechanisms*, Wiley, New York.
[8] Moon, Y., Trease, P., and Kota, S., 2002, "Design of Large-Displacement Compliant Joints," Proceedings of the MECH 27th Biennial Mechanisms and Robotics Conference, Montreal, Canada, Vol. 3.
[9] Deepak, S., Dinesh, M., Sahu, D., and Ananthasuresh, G., 2009, "A Comparative Study of the Formulations and Benchmark Problems for the Topology Optimization of Compliant Mechanisms," ASME J. Mech. Rob., **1**, p. 011003.
[10] Frecker, M., Ananthasuresh, G., Nishiwaki, S., Kikuchi, N., and Kota, S., 1997, "Topological Synthesis of Compliant Mechanisms Using Multi-Criteria Optimization," ASME J. Mech. Des., **119**, pp. 238–245.
[11] Mankame, N., and Ananthasuresh, G., 2004, "Topology Synthesis of Electrothermal Compliant Mechanisms Using Line Elements," Struct. Multidiscip. Optim., **26**, pp. 209–218.
[12] Werme, M., 2007, "Designing Compliant Mechanisms With Stress Constraints Using Sequential Linear Integer Programming," Proceedings of the Seventh World Congress on Structural and Multidisciplinary Optimization, Seoul, South Korea, pp. 1862–1871.
[13] Mechkour, H., Jouve, F., Rotinat-Libersa, C., Bidard, C., and Perrot, Y., 2007, "Optimal Design of Compliant Mechanisms by Level Set and Flexible Building Blocks Methods," Proceedings of the Seventh World Congress on Structural and Multidisciplinary Optimization, Seoul, South Korea, pp. 1898–1907.
[14] Messac, A., Ismail-Yahaya, A., and Mattson, C., 2003, "The Normalized Normal Constraint Method for Generating the Pareto Frontier," Struct. Multidiscip. Optim., **25**(2), pp. 86–98.
[15] De Bona, F., and Munteanu, M. G., 2005, *Optimized Flexural Hinges for Compliant Micromechanisms*, Springer Science, New York, Vol. 44, pp. 163–174.
[16] Cardou, P., and Angeles, J., 2007, "Simplectic Architectures for True Multi-Axial Accelerometers: A Novel Application of Parallel Robots," Proceedings of the IEEE International Conference on Robotics and Automation, Rome, Italy, pp. 181–186.
[17] Kreyszig, E., 1997, *Advanced Engineering Mathematics*, 8th ed., Wiley, New York.
[18] Angeles, J., 2004, "The Qualitative Synthesis of Parallel Manipulators," ASME J. Mech. Des., **126**(4), pp. 617–624.
[19] Derderian, A. M., Howell, L., Murphy, M. D., Lyon, S. M., and Pack, S. D., 1996, "Compliant Parallel-Guiding Mechanisms," Proceedings of the 1996 ASME Design Engineering Technical Conference, Irvine, CA, Vol. 96.
[20] Smith, S., Badami, V., Dale, J., and Xu, Y., 1997, "Elliptical Flexure Hinges," Rev. Sci. Instrum., **68**(3), pp. 1474–1483.
[21] Wu, Y., and Zhou, Z., 2002, "Design Calculations for Flexure Hinges," Rev. Sci. Instrum., **73**(8), pp. 3101–3106
[22] Williams, M., 1952, "Stress Singularities Resulting From Various Boundary Conditions in Angular Corners of Plates in Extension," ASME J. Appl. Mech., **74**, pp. 526–528.
[23] Dunn, M., Suwito, W., and Cunningham, S., 1997, "Stress Intensities at Notch Singularities," Eng. Fract. Mech., **57**(4), pp. 417–430.
[24] Pedersen, P., 2007, "Some Benchmarks for Optimized Shapes With Stress Concentration," Proceedings of the Seventh World Congress on Structural and Multidisciplinary Optimization, Seoul, South Korea, pp. 1623–1631.
[25] Desrochers, S., 2008, "Optimum Design of Simplicial Uniaxial Accelerometers," MS thesis, McGill University, Montreal, Canada.
[26] Neuber, H., 1945, *Theory of Notch Stresses: Principles for Exact Stress Calculation*, Edwards Brothers, Ann Arbor, MI.
[27] Loria, G., 1902, *Spezielle Algebraische und Transscendente Ebene Kurven: Theorie und Geschichte*, BG Teubner, Leipzig.
[28] Gray, A., 1993, *Modern Differential Geometry of Curves and Surfaces*, CRC, Boca Raton, FL.
[29] Khan, W. A., 2007, "The Conceptual Design of Robotic Architectures Using Complexity Criteria," Ph.D. thesis, McGill University, Montreal, Canada.
[30] Nelder, J., and Mead, R., 1965, "A Simplex Method for Function Minimization," Comput. J., **4**, pp. 308–313.
[31] Rahman, M., 2006, "An Intelligent Moving Object Optimization Algorithm for Design Problems With Mixed Variable, Mixed Constraints, and Multiple Objectives," Struct. Multidiscip. Optim., **32**, pp. 40–58.